


Accurate Metasurface Synthesis Incorporating Near-Field Coupling Effects

A.E. Olk^{1,2,*} and D.A. Powell¹

¹*School of Engineering and Information Technology, The University of New South Wales, Canberra, Australia*

²*IEE S.A., ZAE Weiergewan, 11 Rue Edmond Reuter, L-5326 Contern, Luxembourg*

 (Received 18 December 2018; revised manuscript received 7 March 2019; published 4 June 2019)

One of the most promising metasurface architectures for the microwave and terahertz frequency ranges consists of three patterned metallic layers separated by dielectrics. Such metasurfaces are well suited to planar fabrication techniques and their synthesis is facilitated by modeling them as impedance sheets separated by transmission lines. We show that this model can be significantly inaccurate in some cases, due to near-field coupling between metallic layers. This problem is particularly severe for higher frequency designs, where fabrication tolerances prevent the patterns from being highly subwavelength in size. Since the near-field coupling is difficult to describe analytically, correcting for it in a design typically requires numerical optimization. We propose an extension of the widely used equivalent-circuit model to incorporate near-field coupling and show that the extended model can predict the scattering parameters of a metasurface accurately. Based on our extended model, we introduce an improved metasurface synthesis algorithm that gives physical insight to the problem and efficiently compensates for the perturbations induced by near-field coupling. Using the proposed algorithm, a Huygens metasurface for beam refraction is synthesized showing a performance close to the theoretical efficiency limit despite the presence of strong near-field coupling.

DOI: [10.1103/PhysRevApplied.11.064007](https://doi.org/10.1103/PhysRevApplied.11.064007)

I. INTRODUCTION

Metasurfaces are thin sheets of subwavelength resonators, which have emerged as a versatile platform for wavefront manipulation, addressing applications from microwave to visible frequencies [1–3]. Where high transmission efficiency is required, Huygens' metasurfaces are widely used as they feature equal electric and magnetic dipole responses to suppress spurious reflections [4–6]. Different metasurface architectures and corresponding synthesis methods have been proposed within the last two decades [2]. For microwave to terahertz frequencies, most reported work is based on planar stacks of three patterned metallic layers, separated by dielectric substrates, as this architecture is compatible with planar-circuit manufacturing techniques [3,7,8]. In addition to Huygens' metasurfaces, the same approach has been used to realize bianisotropic metasurfaces, which are more efficient for very large refraction angles [9–11].

In synthesizing metasurfaces, it is often necessary to assume that meta-atoms are small compared to the wavelength. This has motivated the development of deeply subwavelength meta-atoms [7,12], with feature sizes on the order of $\lambda/200$. For metasurfaces operating at W-band frequencies (75–110 GHz) and higher, the resulting

feature sizes are too small for conventional printed-circuit-board-fabrication techniques, so simpler geometries such as dogbone [13–15] must be used. This frequency range is of interest for applications such as wireless communication [16] and radar [17,18], and metasurfaces should enable devices such as efficient transmitarray antennas [19,20]. Despite the high potential for applications, there is only one work reporting transmissive refracting metasurfaces operating at W-band frequencies [19]. Efficient modeling of near-field interaction would enable metasurfaces to be synthesized with simpler geometries, which are feasible to fabricate for this frequency range.

In modeling multilayered printed-circuit metasurfaces, each metallic layer is represented by an equivalent surface impedance and the dielectric layers in between are treated as transmission-line sections (see Fig. 1) [5,19,21]. The advantage of this model is that it yields expressions for the required surface impedance of each metallic layer, greatly simplifying the process of designing the metasurface. The transmission-line model accounts for the propagation of the fundamental Floquet harmonic within a periodic metasurface, neglecting all higher-order harmonics, since they are evanescent. Neglecting evanescent waves is accurate for structures with large separation relative to the wavelength, however in metasurfaces it is usually required that the separation between the metallic layers is small. Thus near-field coupling between the layers is neglected. As we

*a.olk@student.adfa.edu.au

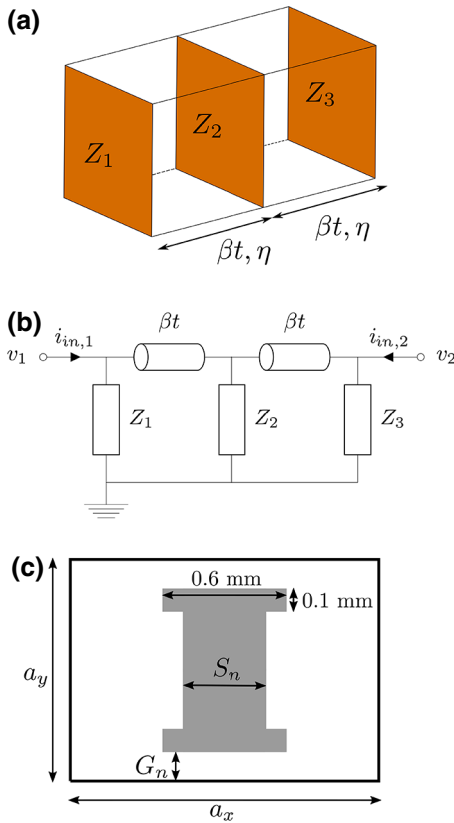


FIG. 1. (a) Cascaded impedance sheets representing a multilayer metasurface and (b) corresponding circuit analogy. (c) Metallic pattern of the dogbone metasurface. The parameters used in this section are $G_1 = G_3 = 126 \mu\text{m}$, $G_2 = 149 \mu\text{m}$, $S_1 = S_3 = 300 \mu\text{m}$, and $S_2 = 400 \mu\text{m}$. The lateral spacing is $a_x = 1.52 \text{ mm}$ and $a_y = 1.09 \text{ mm}$.

show here, this approximation is significantly inaccurate in cases of practical interest, and can lead to performance degradation. Therefore, accurate modeling and synthesis of transmissive metasurfaces must take account of near-field effects between metallic layers. We note that the near-field coupling effects that are investigated here are not related to the evanescent waves (or auxiliary fields) deliberately introduced in Ref. [22].

Early works on near-field interaction in metamaterials aimed to model the propagation of magneto-inductive waves in arrays of split-ring resonators [23], to analyze tunability through modifying lattice parameters [24] and to analyze optical activity of twisted dimers [25,26]. Furthermore, several recent works propose analytical design approaches for metagratings based on rigorous descriptions of the mutual interaction of individual particles [15,27–30]. While these works on near-field coupling in metagratings provide full insight into the interaction of individual scatterers and demonstrate highly efficient devices, they have been largely restricted to reflective operation at large angles. More recently, near-field effects

within and between cells of a metasurface have been investigated in gap plasmon structures [31,32]. For other important metasurface geometries, especially those for operation in transmission, near-field coupling is still largely unexplored and achieving the designed transmission response often requires black-box optimization [10,13] or *ad hoc* iterative design methods [19].

In this paper, we demonstrate how the model of cascaded impedance sheets can be significantly inaccurate due to near-field coupling between metallic layers. We propose an extension of this model to incorporate near-field coupling and show that the extended model can predict the scattering parameters of metasurfaces accurately. This proposed coupling model does not require the explicit calculation of electromagnetic interaction integrals as in previous works [24,26]. The inaccuracies caused by near-field coupling can hamper the synthesis of transmissive multilayer metasurfaces. Therefore, we introduce an improved synthesis algorithm based on the proposed model, which provides good physical insight and reduced computational effort compared to black-box optimization. The algorithm is applied to a homogeneous Huygens metasurface with dogbone resonators, then to an inhomogeneous metasurface exhibiting anomalous refraction.

II. DESIGN OF METASURFACES WITH THREE METALLIC LAYERS

The model of cascaded impedance sheets is widely used in the literature for the analysis of transmissive metasurfaces [5,19,21]. With this model, the properties of each layer are specified based on the scattering properties of the multilayer stack, allowing the synthesis to be reduced to readily solvable problems. However, the model does not account for near-field coupling between layers, which can lead to significant inaccuracy. In the following, we briefly recapitulate the model and show that neglecting near-field coupling can lead to significant inaccuracy in the design of a homogeneous Huygens metasurface.

Each metallic layer is represented by a shunt impedance Z_n and the dielectric layers are represented by a transmission line with propagation constant β , wave impedance $\eta = \sqrt{\mu/\epsilon}$, and thickness t [33] as depicted in Fig. 1(a). Utilizing a circuit analogy, currents are equivalent to the magnetic field and voltages are equivalent to the electric field [33]. The transmission-line model accounts for far-field (or first-order Floquet) coupling between the metallic layers. It is difficult to calculate a meaningful propagation angle within a single meta-atom, therefore within each cell propagation normal to the surface is assumed [21]. The corresponding circuit for the three-layer system is shown in Fig. 1(b). Using this circuit, the network parameters of each cell can be determined by cascading the individual building blocks in terms of transmission (ABCD) matrices $\mathbf{A}_{\text{tot}} = \mathbf{A}_{Z1} \mathbf{A}_{\text{TL}} \mathbf{A}_{Z2} \mathbf{A}_{\text{TL}} \mathbf{A}_{Z3}$, where the transmission matrix

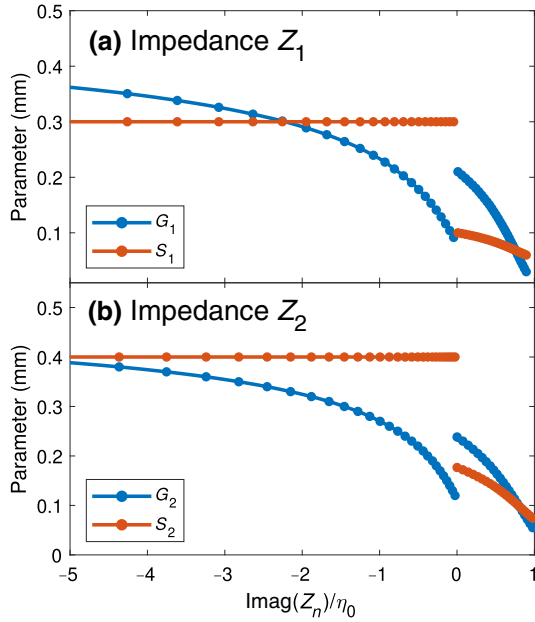


FIG. 2. Lookup table for the dogbone cell. The geometrical parameters are related to the shunt impedance of the (a) outer and (b) inner layers.

of a shunt impedance \mathbf{A}_{Z_n} and a transmission line \mathbf{A}_{TL} are defined in Appendix A. The transmission matrix of the complete cell \mathbf{A}_{tot} is transformed into a scattering matrix \mathbf{S}_{tot} . In Ref. [21] it was shown how the designed transmission response of the cell leads to specification for each of the three sheet impedances shown in Fig. 1. We perform numerical simulations of the dogbone structure to create a lookup table relating its geometric parameters to the sheet impedance Z_n , which is shown in Fig. 2. We note that the relationship between impedance and geometric parameters differs between the inner and outer layers due to the difference in surrounding dielectric medium.

To apply the model, we synthesize one unit cell of a Huygens metasurface for operation in the millimeter wave band at $f_0 = 80$ GHz with the metallic layers having the dogbone geometry depicted in Fig. 1(c). With the smallest metallic feature size of 0.1 mm, a substrate thickness of $t = 254 \mu\text{m}$, and a permittivity of $\epsilon_r = 3.0$, this unit-cell design is compatible with standard printed-circuit-board fabrication while operating at W-band frequencies (similar to Ref. [19]). This results in relatively large resonators, with lateral unit-cell dimensions of $a \gtrsim \lambda/5$. To allow comparison with theory, we assume lossless dielectric layers, and perfectly conducting metal patterns with zero thickness. Since Huygens' metasurfaces are symmetrical, the first and third layers are identical, i.e., $Z_1 = Z_3$, $G_1 = G_3$, and $S_1 = S_3$.

The metasurface is designed to reach near-unity transmission amplitude and a transmission phase response of $\phi_{\text{des}} = 22.9^\circ$ at frequency f_0 . In Fig. 3, the transmission

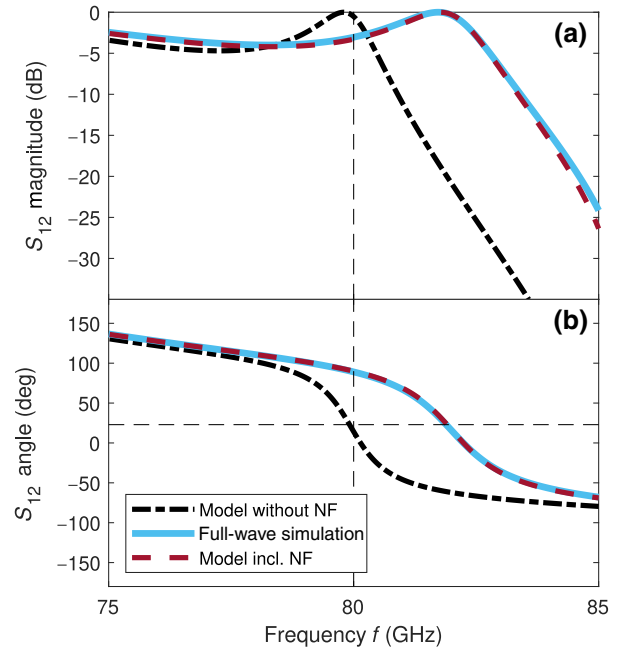


FIG. 3. Transmission (a) magnitude and (b) phase of a Huygens metasurface predicted by the existing model (black dashed curve), showing significant disagreement with full-wave simulation (blue curve). Incorporating near-field coupling between layers (red dashed curve) accurately predicts the response.

response of the model (black dashed line) is compared to results from full-wave simulation (blue solid line). The model predicts that transmission is close to unity amplitude and meets the expected phase ϕ_{des} at f_0 . However, full-wave simulation reveals that the transmission maximum and the corresponding phase are significantly shifted to 81.9 GHz. We attribute this discrepancy to near-field coupling (or equivalently higher-order Floquet modes), which is to be expected, given that $\beta t \ll 1$. This clearly demonstrates that this widely used model can fail for some geometries of practical interest, and consequently it is not precise enough for the synthesis of metasurfaces having high efficiency.

III. MODELING NEAR-FIELD COUPLING BETWEEN LAYERS

Here we extend the model of metasurfaces with three metallic layers to incorporate near-field coupling between the layers. We note that the presented model is quite general and could also be applied to bianisotropic metasurfaces, or to designs containing four or more layers [34–37].

A. Near-field impedance matrix

We extend the circuit model shown in Fig. 1(b) by accounting for the mutual impedance between each of the metallic layers. As shown in Fig. 4, this is represented

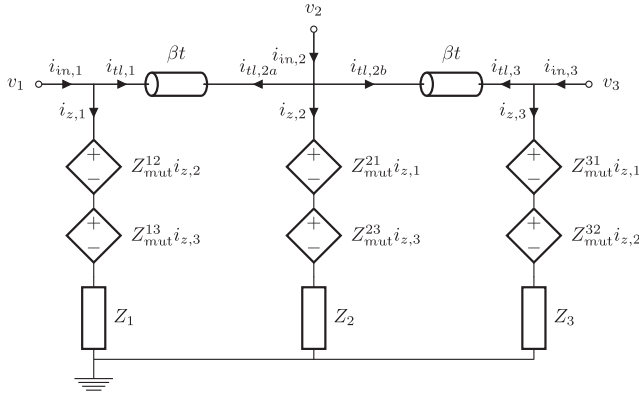


FIG. 4. Proposed equivalent circuit model representing three-layer metasurfaces. Interlayer near-field coupling is included using current-controlled voltage sources.

within the equivalent circuit model by current-controlled voltage sources. To facilitate our analysis, we include a virtual port at the location of the center metallic layer. Consistent with the existing model, we assume that propagation within a single meta-atom is normal to the surface.

We introduce the near-field impedance matrix \mathbf{Z}_{NF} , which gives the near-field relationship between the equivalent voltages v_n and currents $i_{z,n}$ on each of the metallic layers

$$\begin{bmatrix} v_1 \\ v_2 \\ v_3 \end{bmatrix} = \begin{bmatrix} Z_1 & Z_{\text{mut}}^{12} & Z_{\text{mut}}^{13} \\ Z_{\text{mut}}^{21} & Z_2 & Z_{\text{mut}}^{23} \\ Z_{\text{mut}}^{31} & Z_{\text{mut}}^{32} & Z_3 \end{bmatrix} \begin{bmatrix} i_{z,1} \\ i_{z,2} \\ i_{z,3} \end{bmatrix}. \quad (1)$$

The diagonal terms Z_n are the self-impedances of layer n and the off-diagonal elements are the transfer impedances Z_{mut}^{lm} of the corresponding current-controlled voltage sources, hence they represent coefficients that quantify the near-field coupling between layer l and m . We consider only reciprocal structures, therefore \mathbf{Z}_{NF} is a symmetric matrix with $Z_{\text{mut}}^{lm} = Z_{\text{mut}}^{ml}$. Also note that the use of a scalar current $i_{z,n}$ to represent the current flow on a metallic layer is valid so long as only one mode can be excited on it.

To relate \mathbf{Z}_{NF} to the scattering parameters of the entire cell, we first convert it to admittance parameters $\mathbf{Y}_{\text{NF}} = \mathbf{Z}_{\text{NF}}^{-1}$. The admittance matrix of the complete cell \mathbf{Y}_{tot} relates the equivalent current $i_{\text{in},n}$ flowing into each port to the equivalent voltages

$$\begin{bmatrix} i_{\text{in},1} \\ i_{\text{in},2} \\ i_{\text{in},3} \end{bmatrix} = \mathbf{Y}_{\text{tot}} \begin{bmatrix} v_1 \\ v_2 \\ v_3 \end{bmatrix}. \quad (2)$$

Admittance matrix \mathbf{Y}_{FF} represents the far-field contribution of the transmission lines through their equivalent

current $i_{\text{TL},n}$.

$$\begin{bmatrix} i_{\text{TL},1} \\ i_{\text{TL},2} \\ i_{\text{TL},3} \end{bmatrix} = \mathbf{Y}_{\text{FF}} \begin{bmatrix} v_1 \\ v_2 \\ v_3 \end{bmatrix}, \quad (3)$$

where we introduce the total transmission-line current at the central node as $i_{\text{TL},2} = i_{\text{TL},2a} + i_{\text{TL},2b}$. An analytical expression for \mathbf{Y}_{FF} is given in Appendix A.

Using the relation $i_{\text{in},n} = i_{z,n} + i_{\text{TL},n}$ and Eqs. (1)–(3), we can write

$$\mathbf{Y}_{\text{tot}} = \mathbf{Y}_{\text{NF}} + \mathbf{Y}_{\text{FF}}. \quad (4)$$

Using these admittance matrices, near-field and far-field contributions to the interlayer coupling simply sum up and can be linked to the network parameters of the complete cell system \mathbf{Y}_{tot} .

As no current can flow through the virtual port 2 of Fig. 4, we impose the condition $i_{\text{in},2} = 0$. This leads to a reduced admittance matrix \mathbf{Y}'_{tot} for the complete cell, defined as

$$\begin{bmatrix} i_{\text{in},1} \\ i_{\text{in},3} \end{bmatrix} = \mathbf{Y}'_{\text{tot}} \begin{bmatrix} v_1 \\ v_3 \end{bmatrix}, \quad (5)$$

with its relationship to \mathbf{Y}_{tot} shown in Appendix A.

Given a near-field impedance matrix \mathbf{Z}_{NF} , the reduced two-port admittance matrix \mathbf{Y}'_{tot} can be determined using Eqs. (4) and (A4). This is then converted to a scattering matrix \mathbf{S}_{tot} , to obtain transmission and reflection properties of the metasurface. Note that if the near-field coupling coefficients Z_{mut}^{lm} are set to zero, this formalism is equivalent to the existing model outlined in Sec. II.

B. Determination of the near-field impedance terms

To apply the formalism developed in Sec. III A to metasurface analysis, it is necessary to find the values of elements of \mathbf{Z}_{NF} . Since \mathbf{Z}_{NF} is a 3×3 matrix and \mathbf{S}_{tot} is a 2×2 matrix, a single far-field scattering simulation yields insufficient information to resolve \mathbf{Z}_{NF} . Therefore, we propose a technique to determine the elements of \mathbf{Z}_{NF} successively from full-wave simulations of reduced systems containing only two layers. A two-layer formalism analogous to Sec. III A is applied to these full-wave scattering parameters, which allows the unambiguous extraction of individual elements of \mathbf{Z}_{NF} . This two-layer formalism is outlined in Appendix A.

A typical configuration for a full-wave simulation of the unit cell of a metasurface with three layers is shown in Fig. 5(a). The unit cell is centered at $z = 0$, periodic boundary conditions apply to all sides and Floquet ports are located at a large distance d_p to the top and bottom of the structure, where the influence of high-order Floquet modes is negligible. The reference plane of these

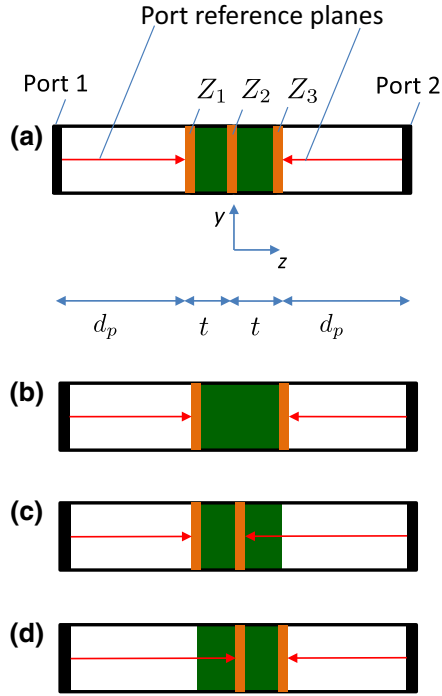


FIG. 5. (a) Cross-sectional layout of a typical full-wave simulation to determine the scattering parameter of a unit cell. (b)–(d) Individual simulations that are required to determine the near-field impedance matrix \mathbf{Z}_{NF} .

ports however needs to be moved back to the top and bottom to $z = \pm t$, respectively, to correct the reflection and transmission phase [7].

By removing the central metallic layer, as shown in Fig. 5(b), the two-layer formalism can be applied to determine the self-impedance of layers one and three, Z_1 and Z_3 , and their mutual impedance Z_{mut}^{13} . To determine Z_1 , Z_2 , and Z_{mut}^{12} , the configuration from Fig. 5(c) is utilized. Here, however, the reference plane of port 2 needs to be moved to the central metal layer, which can be done by inverting the ABCD matrix of the dielectric layer [38]. Similarly, Z_2 , Z_3 , and Z_{mut}^{23} can be obtained from the configuration from Fig. 5(d). Using this successive approach, the full coupling matrix \mathbf{Z}_{NF} is determined and the three-layer system is fully characterized.

We apply this technique to the metasurface considered in Sec. II to determine the near-field impedance matrix \mathbf{Z}_{NF} . As we consider a Huygens metasurface with $Z_1 = Z_3$ and $Z_{\text{mut}}^{1m} = Z_{\text{mut}}^{m1}$, only two simulations are required to determine the near-field impedance matrix \mathbf{Z}_{NF} , since the configurations in Figs. 5(c) and 5(d) are equivalent. The resulting self-impedances Z_n and mutual impedances Z_{mut}^{lm} are shown in Fig. 6. As we consider lossless structures, these functions are purely imaginary to within numerical accuracy [$|\text{Re}(Z)|/\eta_0 < 10^{-5}$]. At the design frequency, the mutual impedance Z_{mut}^{12} and Z_{mut}^{13} are clearly smaller than the self-impedances Z_1 and Z_2 , however they are not

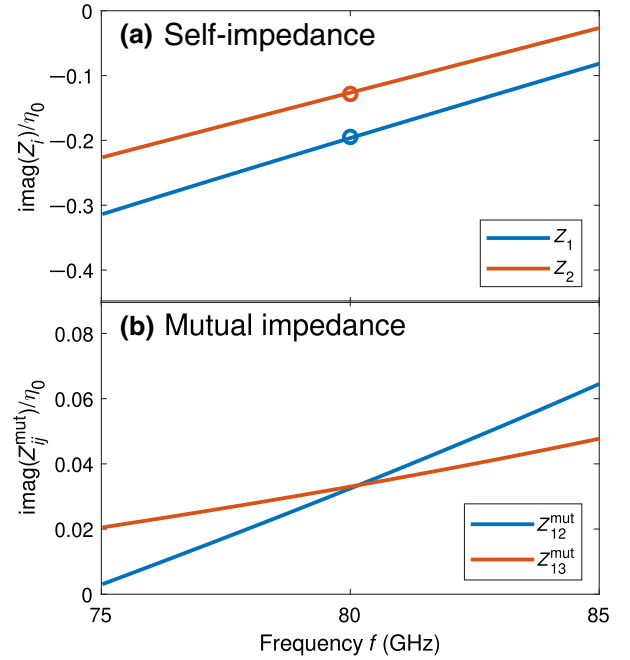


FIG. 6. Extracted values of (a) self-impedance $\text{imag}(Z_n)$ and (b) mutual impedance $\text{imag}(Z_{\text{mut}}^{lm})$ for a three-layer dogbone structure.

negligible. The mutual and self-impedance terms have the form of a series LC circuit. Using the calculated near-field impedance matrix, the metasurface transmission is plotted in Fig. 3 (red dashed line), showing good agreement with the full-wave simulation. This result confirms the accuracy of our near-field coupling model, demonstrating why the conventional metasurface synthesis procedure fails in this case.

IV. METASURFACE SYNTHESIS INCORPORATING NEAR-FIELD COUPLING

A. Refinement algorithm for metasurface synthesis

Having characterized how near-field coupling can render existing metasurface design techniques inaccurate, we present an approach to include it within the metasurface synthesis. Since the near-field coupling cannot be evaluated until a geometry of the metal layer has been specified, this necessarily involves the use of an iterative algorithm. The goal of the algorithm is to find the geometrical parameters of the unit cell that match the target scattering parameters. In the case of Huygens' metasurfaces, it is sufficient to minimize the difference between the realized transmission S_{21}^{re} and designed transmission S_{21}^{des}

$$\min(|S_{21}^{\text{re}} - S_{21}^{\text{des}}|^2). \quad (6)$$

The realized transmission S_{21}^{re} is calculated from our near-field coupling model with the matrix \mathbf{Z}_{NF} . A fundamental assumption of the algorithm is that for small changes of

self-impedances Z_n , the geometric change is small, and the mutual coupling does not change strongly. This allows us to correct only the diagonal elements of the coupling matrix with a factor γ at each iteration

$$\mathbf{Z}_{\text{NF},p} = \mathbf{Z}_{\text{NF},p-1} + \gamma \text{diag}(Z_{1,p-1}, Z_{2,p-1}, Z_{3,p-1}), \quad (7)$$

where the iteration index is denoted with p . The factor γ is chosen by minimizing the term $|S_{12}^{\text{re}}(\mathbf{Z}_{\text{NF},p}) - S_{12}^{\text{des}}|^2$ numerically in each iteration.

Based on the corrected self-impedances $Z_{n,p}$, the geometry of the unit cell is updated with new geometrical parameters G_n and S_n using the lookup table in Fig. 2. If a further iteration is necessary, the mutual impedances are recalculated with full-wave simulations of the new geometry. Note that Eq. (7) could be modified to adjust outer-layer impedances separately from the inner-layer ones, however this is found empirically to offer no improvement in convergence. The optimization process is outlined in full in Algorithm 1.

Initialize: $p = 0$

Start geometry:

Calculate self impedances $Z_{n,p=0}$ from model without near-field coupling and set geometry accordingly

Calculate near-field coupling terms:

Determine $Z_{mut,p=0}^{12}, Z_{mut,p=0}^{13}$ and $Z_{mut,p=0}^{23}$ with full wave simulations obtaining $\mathbf{Z}_{\text{nf},p=0}$

Start iterative steps: $p = 1$

while($p < p_{max}$)

Initialize coupling matrix according to Eq. (7)

Calculate correction factor γ by minimizing $|S_{12}^{\text{re}}(\mathbf{Z}_{\text{nf},p}) - S_{12}^{\text{des}}|^2$ to get new $\mathbf{Z}_{\text{nf},p}$

Update geometry accordingly

if($|\gamma| < \gamma_c$) **then**
terminate

end

Recalculate actual $Z_{mut,p}^{12}, Z_{mut,p}^{13}$ and $Z_{mut,p}^{23}$ with current geometry and update $\mathbf{Z}_{\text{nf},p}$

$p=p+1$

end

Algorithm 1. Refinement algorithm for metasurface synthesis.

The algorithm terminates when the relative change of the self-impedances from one iteration to the next is smaller than γ_c . This convergence parameter is chosen as $\gamma_c = 0.085$ for the examples shown in this work. The absolute value of the resulting correction factor for the self-impedances $|\gamma|$ ranged between 0.038 and 0.25. The ability of this algorithm to correct the transmission response of a cell is shown in Fig. 7. The red dashed line shows the initial response according to the design procedure outlined in Sec. II. The black dash-dot curve shows the result of the model after the optimization, and the blue lines show the corresponding results of full-wave simulation. It can be

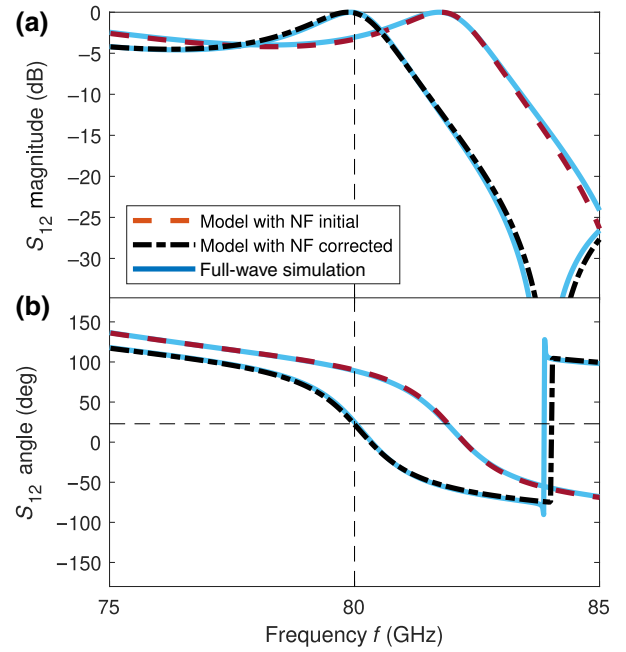


FIG. 7. Transmission of Huygens' metasurface before and after applying the optimization procedure. (a) Transmission magnitude and (b) phase. The thin dashed lines indicate the designed operating frequency and phase response.

seen that the strong perturbation of the operating frequency has been corrected, and the metasurface now achieves complete transmission and the designed phase value at the operating frequency.

B. Application to metasurface demonstrating anomalous refraction

We demonstrate the further utility of our iterative algorithm by applying it to an inhomogeneous Huygens metasurface demonstrating anomalous refraction of a plane wave. The incident angle is chosen $\theta_{\text{in}} = 0$ and the refraction angle $\theta_{\text{out}} = 55^\circ$, leading to a supercell width $d = 4.56$ mm. Each cell is based on the dogbone geometry shown in Fig. 1(a). To minimize the influence of coupling to nonidentical neighboring cells, which is not described in our model, the lateral spacing a_x is chosen as large as possible. With the supercell width used here, there are three propagating Floquet modes in transmission, T_0 and $T_{\pm 1}$, and three in reflection R_0 and $R_{\pm 1}$. To control these 6 degrees of freedom, a minimum of three cells per supercell is required, each having an engineered electric and magnetic response.

The initial sheet impedances $Z_{n,p=0}$ and the required transmission response for each cell S_{21}^{des} are specified according to the design procedure in Ref. [7]. With these target values, impedance matching to the refracted wave is stipulated. The geometry of each cell is synthesized using the algorithm from Sec. IV A. The self-impedance $Z_{n,p}$ of

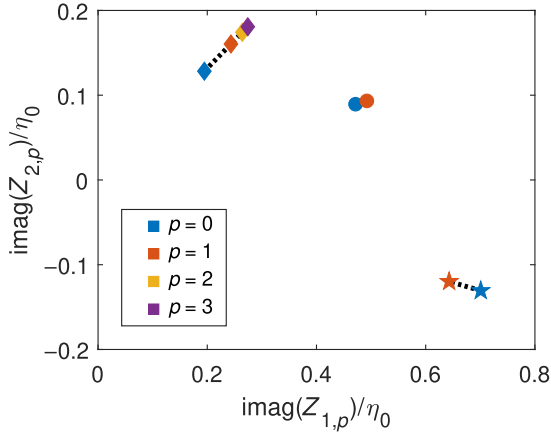


FIG. 8. Self-impedances of each layer $Z_{n,p}$ at iteration step p . The marker shapes \diamond , \circ , and \star indicate cell 1, 2, and 3 respectively.

each cell n at iteration p is shown in Fig. 8. In the case of the first cell, having identical geometry to that is analyzed in Sec. II, three iterations are necessary to obtain the required scattering properties. For the other two cells, one iteration is enough, due to the lesser influence of near-field coupling in these cases. The resulting geometrical parameters of the supercell are given in Table I.

We note that an alternative approach to correct for near-field coupling is to use black-box optimization methods, which are built in to many commercial simulation packages. Compared to these methods, our proposed algorithm has several advantages. Unlike these black-box optimization methods, our approach gives clear physical insight into the near-field coupling, which causes the metasurface design to be nonoptimal. In particular, with the quantities Z_{nm}^{mut} , near-field coupling effects can be quantified and monitored from iteration to iteration. Additionally, our algorithm is much more computationally efficient, as is demonstrated by the results in Appendix B, which demonstrates a speed-up factor of 3.6 for the design considered. For metasurface designs with a large number of cells, this speed up would also be a significant benefit. Furthermore, using the proposed algorithm, the influence of near-field coupling effects can be corrected without any prior knowledge. Applying black-box optimization methods requires guessing the required geometric parameter changes and setting suitable parameter boundaries.

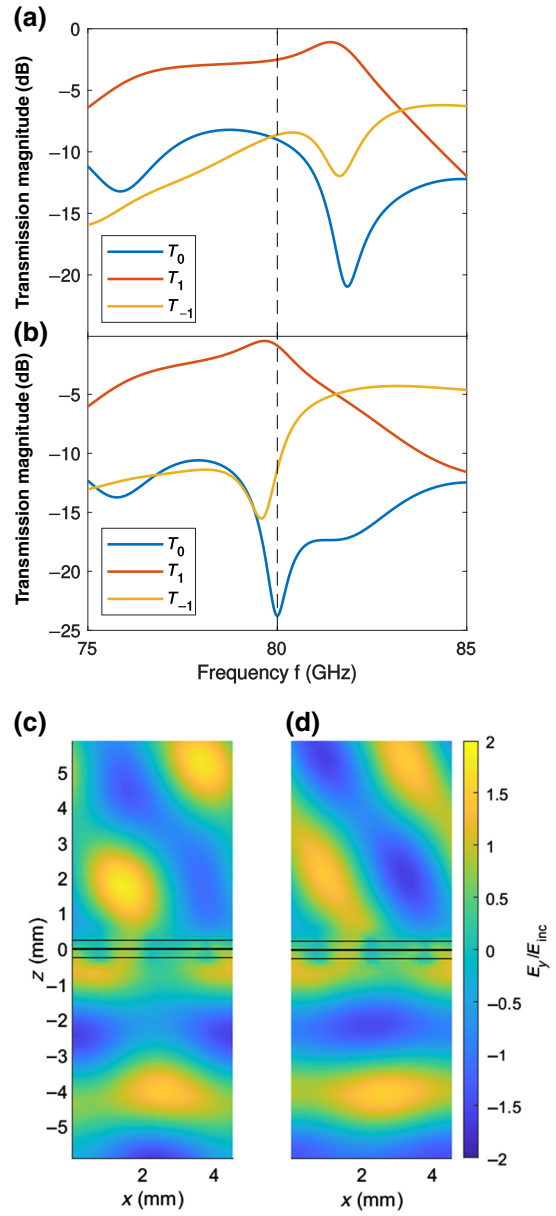


FIG. 9. Performance of the beam-refraction metasurface. Transmission Floquet modes (a) before and (b) after the model-based optimization. Electric field at design frequency $f_0 = 80$ GHz (c) before and (d) after the model-based optimization.

While we consider only a single polarization in this work, we expect that our method could be adapted to tensorial impedances [39] used to model polarization rotating

TABLE I. Geometric parameters of the cells in the refracting metasurface.

Cell	Geometry parameters [μm]											
	1				2				3			
Parameter	S_1	G_1	S_2	G_2	S_1	G_1	S_2	G_2	S_1	G_1	S_2	G_2
Before	300	126	400	149	300	204	172	220	300	175	400	138
After	300	114	400	139	300	210	172	218	300	172	400	137

metasurfaces. We note that for chiral metasurfaces based on coupled high-symmetry layers [40], polarization rotation only occurs when near-field coupling is strong, thus near-field coupling cannot be neglected in equivalent circuit modeling.

The refraction performance of the synthesized metasurface is shown in Fig. 9, where T_1 , the transmission coefficient into the designed Floquet mode, should be maximized, and other terms minimized. The performance of the initial geometry (a) is compared with the performance of the geometry obtained by our iterative optimization process (b). For the initial metasurface, the energy refracted into the desired Floquet mode is as low as 56% at the design frequency $f_0 = 80$ GHz. The maximum refraction efficiency is 78%, but it is significantly shifted to 81.4 GHz. The optimized metasurface on the other hand refracts 82% into the desired Floquet mode T_1 at the design frequency. In this case, the maximum refraction efficiency is 90% at 79.7 GHz. We note that the maximum efficiency of the optimized metasurface is close to the theoretical efficiency limit [7] for Huygens' metasurfaces, which is 92% for a refraction angle of 55° .

V. CONCLUSION

We show that metasurfaces based on patterned metallic layers separated by dielectric layers can exhibit strong interlayer near-field coupling. This can lead to significant inaccuracy of existing models used for metasurface synthesis, resulting in poor performance of the metasurfaces. We develop an improved model, which accounts for near-field coupling and show that it closely matches the results of full-wave simulation. This is of particular significance for higher-frequency designs, where fabrication tolerances mean that feature sizes are not highly subwavelength, leading to strong near-field coupling.

To mitigate the performance degradation induced by near-field coupling, we introduce an iterative algorithm for accurate metasurface synthesis, which takes it into account. The presented algorithm gives more physical insight into the problem than black-box optimization, and reduces computation time significantly. Additionally, it is very generic and can be applied to multilayer metasurfaces in various frequency ranges. As this work introduces an efficient synthesis method for such geometries, it helps to relax fabrication requirements and pave avenues for new metasurface geometries.

ACKNOWLEDGMENTS

This work is financially supported by the Australian Research Council (Linkage Project LP160100253) and the Luxembourg Ministry of the Economy (Grant No. CVN 18/17/RED).

APPENDIX A: TWO- AND THREE-PORT MATRIX REPRESENTATIONS

The ABCD matrices of a shunt impedance \mathbf{A}_{Z_n} and transmission line \mathbf{A}_{TL} [38] are given by

$$\mathbf{A}_{Z_n} = \begin{bmatrix} 1 & 0 \\ 1/Z_n & 1 \end{bmatrix} \quad (\text{A1})$$

and

$$\mathbf{A}_{TL} = \begin{bmatrix} \cos(\beta t) & j\eta \sin(\beta t) \\ j1/\eta \sin(\beta t) & \cos(\beta t) \end{bmatrix}. \quad (\text{A2})$$

The admittance matrix \mathbf{Y}_{FF} for the three-layer system can be determined analyzing the circuit from Fig. 4(b) without shunt elements and dependent sources utilizing the definition of an admittance matrix element $Y_{FF,lm} = i_{TL,l}/v_m |_{v_{k \neq m} = 0}$ and states

$$\mathbf{Y}_{FF} = \begin{bmatrix} \frac{-i}{\eta \tan \beta t} & \frac{i}{\eta \sin \beta t} & 0 \\ \frac{i}{\eta \sin \beta t} & \frac{-2i}{\eta \tan \beta t} & \frac{i}{\eta \sin \beta t} \\ 0 & \frac{i}{\eta \sin \beta t} & \frac{-i}{\eta \tan \beta t} \end{bmatrix}. \quad (\text{A3})$$

To reduce the three-port equivalent circuit shown in Fig. 4 to a two-port network compatible with circuit simulations, we impose the condition $i_{in,2} = 0$. This yields the following expression for the two-port matrix \mathbf{Y}'_{tot} in terms of elements of the three-port matrix \mathbf{Y}_{tot}

$$\mathbf{Y}'_{tot} = \begin{pmatrix} Y_{tot,11} - \frac{Y_{tot,21}}{Y_{tot,22}} Y_{tot,12} & Y_{tot,13} - \frac{Y_{tot,23}}{Y_{tot,22}} Y_{tot,12} \\ Y_{tot,31} - \frac{Y_{tot,21}}{Y_{tot,22}} Y_{tot,32} & Y_{tot,33} - \frac{Y_{tot,23}}{Y_{tot,22}} Y_{tot,32} \end{pmatrix}. \quad (\text{A4})$$

Equations (1)–(4) can be defined analogously for the two-layer system using the 2×2 matrices \mathbf{Y}_{tot}^2 , \mathbf{Y}_{NF}^2 , and \mathbf{Y}_{FF}^2 . In the corresponding circuit model in Fig. 10, the admittance matrix for the transmission line is

$$\mathbf{Y}_{FF}^2 = \begin{pmatrix} \frac{-j}{\eta \tan \beta t} & \frac{j}{\eta \sin \beta t} \\ \frac{j}{\eta \sin \beta t} & \frac{-j}{\eta \tan \beta t} \end{pmatrix}. \quad (\text{A5})$$

With known admittance matrix \mathbf{Y}_{tot}^2 , we can determine $\mathbf{Z}_{NF}^2 = \mathbf{Y}_{NF}^2{}^{-1}$ without any ambiguity. The coefficients of \mathbf{Z}_{NF}^2 for configuration (b)–(d) in Fig. 5 are then used subsequently to build the 3×3 matrix \mathbf{Z}_{NF} . Note, that in configuration (b), the thickness is $2t$.

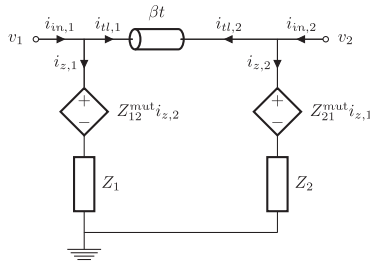


FIG. 10. Equivalent circuit for a two-layer structure.

APPENDIX B: COMPUTATIONAL EFFICIENCY

To evaluate the computation time of the algorithm proposed in this work, it is compared with a black-box trusted-region framework algorithm implemented in the commercial package CST Microwave Studio [41]. The merit function for the optimization is $f_m = |S_{12}^{re} - S_{12}^{des}|^2$, as previously. By far the most significant contribution to the computation time comes from full-wave simulations. Therefore, we compare here the number of full-wave simulations n_{FW} that is required until the respective optimization algorithm converges for both of these methods. Since two full-wave simulations are required to determine the near-field impedance matrix Z_{NF} , the proposed model-based optimization requires $n_{FW} = 2p_t$ when terminating at iteration p_t . The black-box optimization on the other hand requires $n_{FW} = p_t + 1$.

In Fig. 11, the computational effort for the two algorithms is compared in terms of n_{FW} , for each of the three cells in our anomalously refracting metasurface. Our proposed optimization technique is on average 3.6 times faster than the black-box optimization. Additionally, the trusted-region optimization requires some prior knowledge to set the boundaries of the parameter space. Here, we choose $\pm 25\%$ on the initial parameter set.

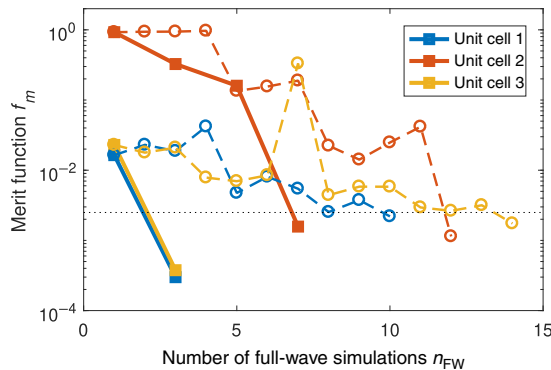


FIG. 11. Comparison of the computation effort of the proposed model-based optimization (solid lines with squares) and a black-box optimization algorithm (dashed lines with circles).

- [1] Nanfang Yu and Federico Capasso, Flat optics with designer metasurfaces, *Nat. Mater.* **13**, 139 (2014).
- [2] Fei Ding, Anders Pors, and Sergey I. Bozhevolnyi, Gradient metasurfaces: A review of fundamentals and applications, *Rep. Progr. Phys.* **81**, 026401 (2018).
- [3] Michael Chen, Minseok Kim, Alex M. H. Wong, and George V. Eleftheriades, Huygens’ metasurfaces from microwaves to optics: A review, *Nanophotonics* **7**, 1207 (2018).
- [4] Carl Pfeiffer and Anthony Grbic, Metamaterial Huygens’ Surfaces: Tailoring Wave Fronts with Reflectionless Sheets, *Phys. Rev. Lett.* **110**, 197401 (2013).
- [5] Francesco Monticone, Nasim Mohammadi Estakhri, and Andrea Alù, Full Control of Nanoscale Optical Transmission with a Composite Metascreen, *Phys. Rev. Lett.* **110**, 203903 (2013).
- [6] Manuel Decker, Isabelle Staude, Matthias Falkner, Jason Dominguez, Dragomir N. Neshev, Igal Brener, Thomas Pertsch, and Yuri S. Kivshar, High-efficiency dielectric Huygens’ surfaces, *Adv. Opt. Mater.* **3**, 813 (2015).
- [7] Ariel Epstein and George V. Eleftheriades, Huygens’ metasurfaces via the equivalence principle: Design and applications, *J. Opt. Soc. Am. B* **33**, A31 (2016).
- [8] Carl Pfeiffer and Anthony Grbic, Bianisotropic Metasurfaces for Optimal Polarization Control: Analysis and Synthesis, *Phys. Rev. Appl.* **2**, 044011 (2014).
- [9] Joseph P. S. Wong, Ariel Epstein, and George V. Eleftheriades, Reflectionless wide-angle refracting metasurfaces, *IEEE Antennas. Wirel. Propag. Lett.* **15**, 1293 (2016).
- [10] Michael A. Cole, Aristeidis Lamprianidis, Ilya V. Shadrivov, and David A. Powell, Refraction efficiency of Huygens’ and bianisotropic terahertz metasurfaces, arXiv:1812.04725 [physics] (2018).
- [11] Ashif A. Fathnan and David A. Powell, Bandwidth and size limits of achromatic printed-circuit metasurfaces, *Opt. Express* **26**, 29440 (2018).
- [12] Joseph P. S. Wong, Michael Selvanayagam, and George V. Eleftheriades, Design of unit cells and demonstration of methods for synthesizing Huygens metasurfaces, *Photon. Nanostruct. Fundam. Appl. Metamater.-2013 Congr.* **12**, 360 (2014).
- [13] G. Lavigne, K. Achouri, V. S. Asadchy, S. A. Tretyakov, and C. Caloz, Susceptibility derivation and experimental demonstration of refracting metasurfaces without spurious diffraction, *IEEE Trans. Antennas. Propag.* **66**, 1321 (2018).
- [14] Filippo Capolino, Andrea Vallecchi, and Matteo Albani, Equivalent transmission line model with a lumped X-circuit for a metalayer made of pairs of planar conductors, *IEEE Trans. Antennas. Propag.* **61**, 852 (2013).
- [15] Oshri Rabinovich and Ariel Epstein, Analytical design of printed-circuit-board (PCB) metagratings for perfect anomalous reflection, *IEEE Trans. Antennas. Propag.* **66**, 4086 (2018).
- [16] Theodore S. Rappaport, Yunchou Xing, George R. MacCartney, Andreas F. Molisch, Evangelos Mellios, and Jianhua Zhang, Overview of millimeter wave communications for fifth-generation (5G) wireless networks with a focus

- on propagation models, *IEEE Trans. Antennas. Propag.* **65**, 6213 (2017).
- [17] S. M. Patole, M. Torlak, D. Wang, and M. Ali, Automotive radars: A review of signal processing techniques, *IEEE Signal. Process. Mag.* **34**, 22 (2017).
- [18] J. Hasch, E. Topak, R. Schnabel, T. Zwick, R. Weigel, and C. Waldschmidt, Millimeter-wave technology for automotive radar sensors in the 77 GHz frequency band, *IEEE Trans. Microw. Theory. Tech.* **60**, 845 (2012).
- [19] C. Pfeiffer and A. Grbic, Millimeter-wave transmitarrays for wavefront and polarization control, *IEEE Trans. Microw. Theory. Tech.* **61**, 4407 (2013).
- [20] Zhi Hao Jiang, Lei Kang, Wei Hong, and Douglas H. Werner, Highly Efficient Broadband Multiplexed Millimeter-Wave Vortices from Metasurface-Enabled Transmit-Arrays of Subwavelength Thickness, *Phys. Rev. Appl.* **9**, 064009 (2018).
- [21] Ariel Epstein and George V. Eleftheriades, Arbitrary power-conserving field transformations with passive lossless omega-type bianisotropic metasurfaces, *IEEE Trans. Antennas. Propag.* **64**, 3880 (2016).
- [22] Ariel Epstein and George V. Eleftheriades, Synthesis of Passive Lossless Metasurfaces Using Auxiliary Fields for Reflectionless Beam Splitting and Perfect Reflection, *Phys. Rev. Lett.* **117**, 256103 (2016).
- [23] R. R. A. Syms, Ekaterina Shamonina, V. Kalinin, and L. Solymar, A theory of metamaterials based on periodically loaded transmission lines: Interaction between magnetoinductive and electromagnetic waves, *J. Appl. Phys.* **97**, 064909 (2005).
- [24] David A. Powell, Mikhail Lapine, Maxim V. Gorkunov, Ilya V. Shadrivov, and Yuri S. Kivshar, Metamaterial tuning by manipulation of near-field interaction, *Phys. Rev. B* **82**, 155128 (2010).
- [25] H. Liu, D. Genov, D. Wu, Y. Liu, Z. Liu, C. Sun, S. Zhu, and X. Zhang, Magnetic plasmon hybridization and optical activity at optical frequencies in metallic nanostructures, *Phys. Rev. B* **76**, 073101 (2007).
- [26] Mingkai Liu, David A. Powell, Ilya V. Shadrivov, and Yuri S. Kivshar, Optical activity and coupling in twisted dimer meta-atoms, *Appl. Phys. Lett.* **100**, 111114 (2012).
- [27] H. Chalabi, Y. Ra'di, D. L. Sounas, and A. Alù, Efficient anomalous reflection through near-field interactions in metasurfaces, *Phys. Rev. B* **96**, 075432 (2017).
- [28] Younes Ra'di, Dimitrios L. Sounas, and Andrea Alù, Metagratings: Beyond the Limits of Graded Metasurfaces for Wave Front Control, *Phys. Rev. Lett.* **119**, 067404 (2017).
- [29] Vladislav Popov, Fabrice Boust, and Shah Nawaz Burokur, Controlling Diffraction Patterns with Metagratings, *Phys. Rev. Appl.* **10**, 011002 (2018).
- [30] Ariel Epstein and Oshri Rabinovich, Perfect Anomalous Refraction with Metagratings, arXiv:1804.02362 [physics] (2018).
- [31] Rucha Deshpande, Vladimir A. Zenin, Fei Ding, N. Asger Mortensen, and Sergey I. Bozhevolnyi, Direct characterization of near-field coupling in gap plasmon-based metasurfaces, *Nano Lett.* **18**, 6265 (2018).
- [32] Nicholas Sharac, Alexander J. Giles, Keith Perkins, Joseph Tischler, Francisco Bezares, Sharka M. Prokes, Thomas G. Folland, Orest J. Glembocki, and Joshua D. Caldwell, Implementation of plasmonic band structure to understand polariton hybridization within metamaterials, *Opt. Express* **26**, 29363 (2018).
- [33] Sergei Tretyakov, *Analytical Methods in Applied Electrodynamics* (Artech House, Boston Massachusetts, 2003).
- [34] Elena Abdo-Sanchez, Michael Chen, Ariel Epstein, and George V. Eleftheriades, A leaky-wave antenna with controlled radiation using a bianisotropic Huygens' metasurface, *IEEE Trans. Antennas. Propag.* **67**, 108 (2019).
- [35] Chuanbao Liu, Yang Bai, Qian Zhao, Yihao Yang, Hongsheng Chen, Ji Zhou, and Lijie Qiao, Fully controllable pancharatnam-berry metasurface array with high conversion efficiency and broad bandwidth, *Sci. Rep.* **6**, 34819 (2016).
- [36] Weikang Pan, Tong Cai, Shiwei Tang, Lei Zhou, and Jianfeng Dong, Trifunctional metasurfaces: Concept and characterizations, *Opt. Express* **26**, 17447 (2018).
- [37] Shan Jiang, Chang Chen, Hualiang Zhang, and Weidong Chen, Achromatic electromagnetic metasurface for generating a vortex wave with orbital angular momentum (OAM), *Opt. Express* **26**, 6466 (2018).
- [38] David M. Pozar, *Microwave Engineering* (Wiley, New Jersey, 2011), 4th ed.
- [39] M. Selvanayagam, and G. V. Eleftheriades, Design and measurement of tensor impedance transmitarrays for chiral polarization control, *IEEE Trans. Microw. Theory. Tech.* **64**, 414 (2016).
- [40] Kirsty Hannam, David A. Powell, Ilya V. Shadrivov, and Yuri S. Kivshar, Broadband chiral metamaterials with large optical activity, *Phys. Rev. B* **89**, 125105 (2014).
- [41] CST Microwave Studio, Darmstadt – Germany (2018).